Remote Chemical Sensing Using Nuclear Spectroscopy

Thomas H. Prettyman
Los Alamos National Laboratory,
Los Alamos, New Mexico

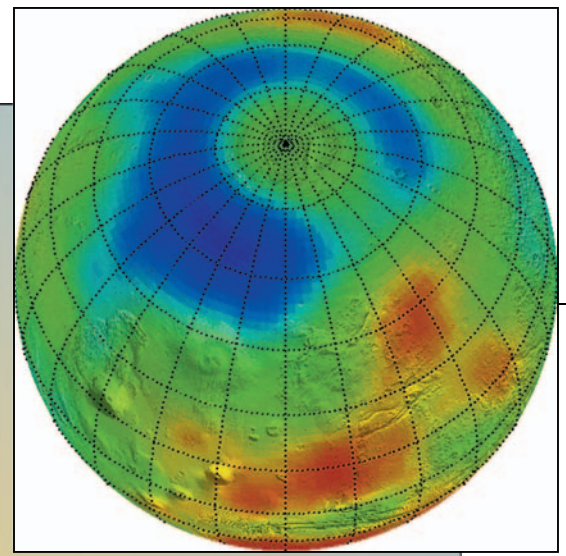

CHAPTER 41

1. Introduction
2. Origin of gamma rays and neutrons
3. Instrumentation
4. Missions
5. Science
6. Future Prospects
Bibliography

1. Introduction

Nuclear spectroscopy techniques are used to determine the elemental composition of planetary surfaces and atmospheres. Radiation, including gamma rays and neutrons, is produced steadily by cosmic ray bombardment of the surfaces and atmospheres of planetary bodies and by the decay of radionuclides within the solid surface. The leakage **flux** of gamma rays and neutrons contains information about the abundance of major elements, selected trace elements, and light elements such as H and C. Gamma rays and neutrons can be measured from high altitudes (less than a planetary radius), enabling global mapping of elemental composition by an orbiting spacecraft. Radiation that escapes into space originates from shallow depths (<1 m within the solid surface). Consequently, nuclear spectroscopy is complementary to other surface mapping techniques, such as reflectance spectroscopy, which is used to determine the mineralogy of planetary surfaces.

The main benefit of gamma ray and neutron spectroscopy is the ability to reliably identify elements important to planetary geochemistry and to accurately determine their abundance. This information can be combined with other remote sensing data, including surface thermal inertia and mineralogy, to investigate many aspects of planetary science. This article provides an overview of this burgeoning area of remote sensing. The origin of gamma rays and neutrons, their information content, measurement techniques, and scientific results from the *Lunar Prospector* and *Mars Odyssey* missions are described.

Nuclear reactions and radioactive decay result in the emission of gamma rays with discrete energies, which provide a fingerprint that can uniquely identify specific elements in the surface. Depending on the composition of the surface, the abundance of major rock-forming elements, such as O, Mg, Al, Si, Cl, Ca, Ti, Fe, and radioactive trace elements, such as K, Th, and U can be determined from measurements of the gamma ray spectrum. The geochemical data provided by nuclear spectroscopy can be used to investigate a wide range of topics, including the following:

- Determining bulk composition for comparative studies of planetary geochemistry and the investigation of theories of planetary origins and evolution;
- Constraining planetary structure and differentiation processes by measuring large-scale stratigraphic variations within impact basins that probe the crust and mantle;
- Characterization of regional scale geological units, such as lunar mare and highlands;
- Estimating the global heat balance by measuring the abundance of radioisotopes such as K, Th, and U;

Encyclopedia of the Solar System 2e ©2007 by Academic Press. All rights of reproduction in any form reserved.

- Measuring the ratio of the volatile element K to the refractory element Th to determine the depletion of volatile elements in the source material from which planets were accreted and to estimate the volatile inventory of the terrestrial planets.

Neutrons are produced by cosmic ray interactions and are sensitive to the presence of light elements within planetary surfaces and atmospheres, including H, C, and N, which are the major constituents of ices as well as elements such as Gd and Sm, which are strong neutron absorbers. In addition, alpha particles are produced by radioactive decay of heavy elements such as U and Th and have been used to identify radon emissions from the lunar surface, possibly associated with tectonic activity.

Close proximity to the planetary body is needed to measure neutrons and gamma rays because their production rate is relatively low. Unlike optical techniques, distances closer than a few hundred kilometers are needed in order to obtain a strong signal. In addition, sensors used for gamma ray and neutron spectroscopy are generally insensitive to incident direction. Consequently, spatial resolution depends on orbital altitude, and higher resolution can be achieved by moving closer to the planet. Regional scale measurements are generally achieved using nuclear spectroscopy, in contrast to the meter to kilometer scale generally achieved by optical remote sensing methods.

Measurements of the solid surface are not possible for planets with thick atmospheres, including the Earth, Venus, and outer planets other than Pluto. Variations in atmospheric composition can be measured and have important implications to understanding seasonal weather patterns. Gamma ray and neutron spectroscopy can be applied to investigate the surfaces of planets with thin atmospheres, such as Mercury, Mars, the Moon, comets, and asteroids. In principle, the satellites of Jupiter and Saturn could be investigated using nuclear spectroscopy; however, the intense radiation environment within the magnetospheres of these planets may be a limiting factor.

X-ray spectroscopy can also be used to determine elemental composition and is complementary to nuclear spectroscopy. Intense bursts of x-rays produced by solar flares cause planetary surfaces to fluoresce. The characteristic x-rays that are emitted can be analyzed to determine the abundance of rock-forming elements such as Fe and Mg. In contrast to nuclear spectroscopy, surface coverage may be limited, especially when solar activity is low; however, high statistical precision for elemental abundances can be achieved during flares. The depth sensitivity of x-ray and nuclear spectroscopy is very different. X-rays are produced much closer to the surface than gamma rays and neutrons. Missions that have used x-ray spectroscopy include *Apollo* and *NEAR* [see Near-Earth Asteroids], and *SMART-1*. The *MESSENGER* mission will use both x-ray and nuclear spectrometers to determine the elemental composition of Mercury, and an x-ray spectrometer will be on the payload of *Chandrayaan-1*, the Indian Space Research Organization's first mission to the Moon.

2. Origin of Gamma Rays and Neutrons

Neutrons and gamma rays are produced by the interaction of energetic particles and cosmic rays with planetary surfaces and atmospheres. While solar energetic particle events can produce copious gamma rays and neutrons, we will focus our attention on **galactic cosmic rays**, which are somewhat higher in energy, penetrate more deeply into the surface, and have a constant flux over relatively long periods of time. **Gamma rays** are also produced steadily by the decay of radioactive elements such as K, Th, and U. A diagram of production and transport processes for neutrons and gamma rays is shown in Fig. 1.

2.1 Galactic Cosmic Rays

Galactic cosmic rays consist primarily of protons with an average flux of about 4 protons per cm^2 per s and with a wide distribution of energies extending to many GeV (Fig. 2; inset). The flux and energy distribution of galactic protons reaching a planetary surface is modulated by the solar cycle [see The Sun]. Sunspot counts are a measure of solar activity (Fig. 2). Higher fluxes of galactic protons are observed during periods of low solar activity. In addition, more low-energy protons penetrate the heliosphere during solar minimum, resulting in a shift in the population towards lower energies. The flux and energy distribution of the cosmic rays are controlling factors in the production rate, energy distribution, and depth of production of **neutrons** and gamma rays. For example, the neutron counting rates at MacMurdo Station in Antarctica are modulated by the solar cycle as shown in Fig. 2.

The GeV-scale energy of galactic protons can be compared to the relatively small binding energy of protons and neutrons in the nucleus (for example, 8.8 MeV/nucleon for ^{56}Fe). High energy interactions with nuclei can be modeled as an intranuclear cascade, in which the energy of the incident particle is transferred to the nucleons, resulting in the emission of secondary particles by spallation, followed by evaporation, and subsequent de-excitation of the residual nuclei. The secondary particles, which include neutrons and protons, undergo additional reactions with nuclei until the initial energy of the cosmic ray is absorbed by the medium. Since most of the gamma ray production is caused by reactions with neutrons, we will focus our attention on how neutrons slow down in matter.

2.2 Fundamentals of Neutron Moderation

Neutrons transfer their energy to the medium through successive interactions with nuclei and are eventually absorbed

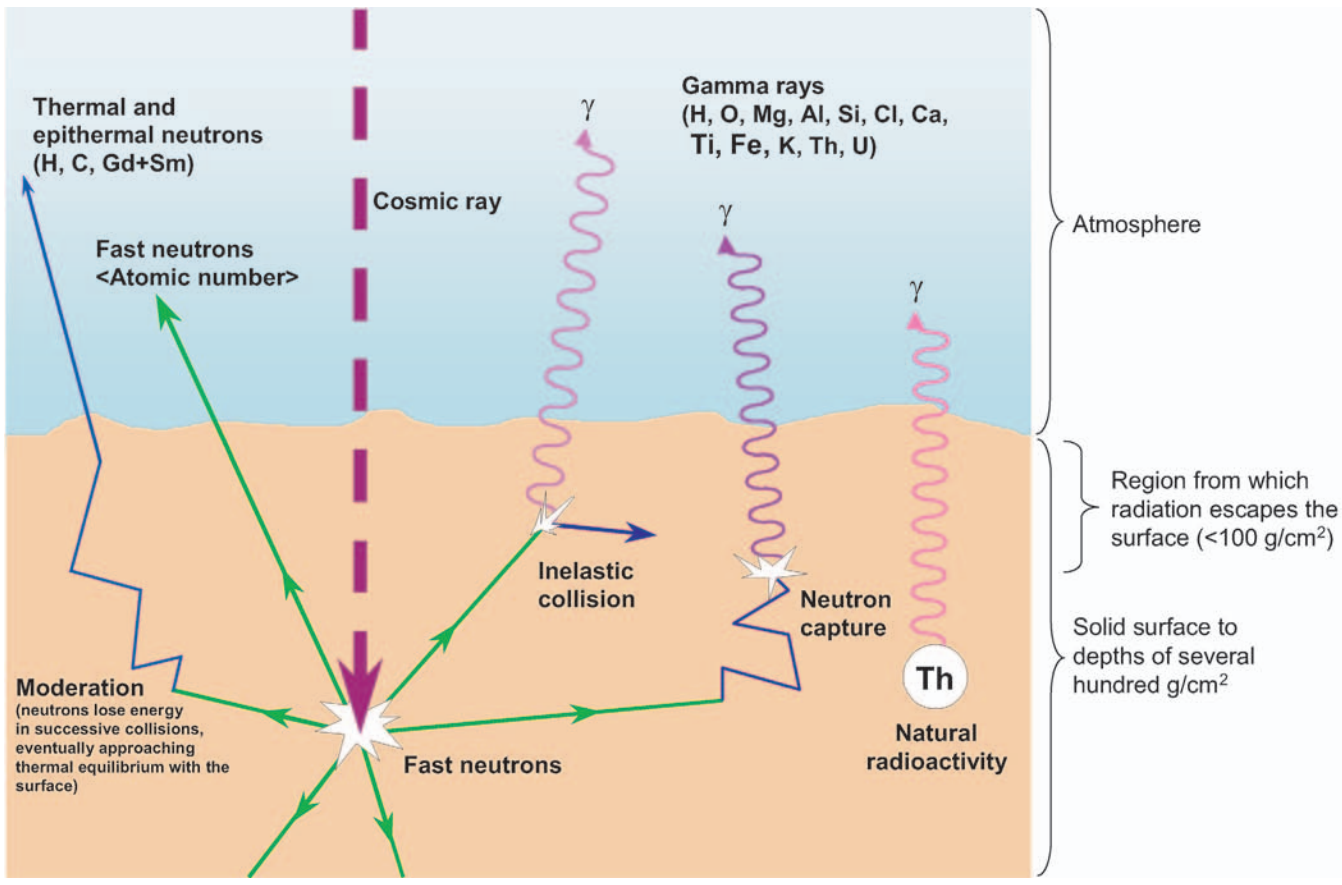

FIGURE 1 Overview of the production of gamma rays and neutrons by cosmic ray interactions and radioactive decay. Fast neutrons produced by high-energy cosmic ray interactions undergo inelastic collisions, resulting in the production of characteristic gamma rays that can be measured from orbit. Neutrons lose energy through successive collisions with nuclei and approach thermal equilibrium with the surface. Thermal and epithermal neutrons provide information about the abundance of light elements, such as H and C, and strong thermal neutron absorbers, such as Gd and Sm. Fast neutrons are sensitive to the average atomic mass of the surface. Gamma rays produced by neutron capture and inelastic scattering can be used to measure the abundance of rock-forming elements, such as O and Fe. Gamma rays are also produced by the decay of long-lived radioisotopes, including K, Th, and U. While cosmic rays can penetrate deep into the surface, the radiation escaping the surface originates from shallow depths, generally less than 100 g/cm^2.

in the surface or atmosphere or escape into space. The process of slowing-down via repeated collisions is known as "moderation." There are three general interaction categories that are important in the context of planetary science: (1) nonelastic reactions, in which the incident neutron is absorbed, forming a compound nucleus, which decays by emitting one or more neutrons followed by the emission of gamma rays; (2) elastic scattering, a process that can be compared to billiard ball collisions for which kinetic energy is conserved; (3) neutron radiative capture, in which the neutron is absorbed and gamma rays are emitted.

The probability that a neutron will interact with a nucleus can be expressed in terms of an effective area of the target nucleus, known as the microscopic cross section, σ, which depends on the energy of the neutron (E) and has units of barns. One barn is 10^{-24} cm^2. Microscopic cross sections for natural Fe are shown, for example, in Fig. 3 for radiative capture, elastic scattering, and inelastic scattering. Inelastic scattering occurs above a threshold determined by the energy required to produce the first excited state of the compound nucleus. The elastic scattering cross section is constant over a wide range of energies. The cross section for radiative capture usually varies as $E^{-1/2}$. Consequently, radiative capture is important at low energies. The sharp peaks that appear at high energy (greater than 100 eV) are resonances associated with the nuclear structure of the Fe isotopes. Neutron inelastic scattering is an important energy loss mechanism at high energies (greater than about 0.5 MeV for most isotopes of interest to planetary science).

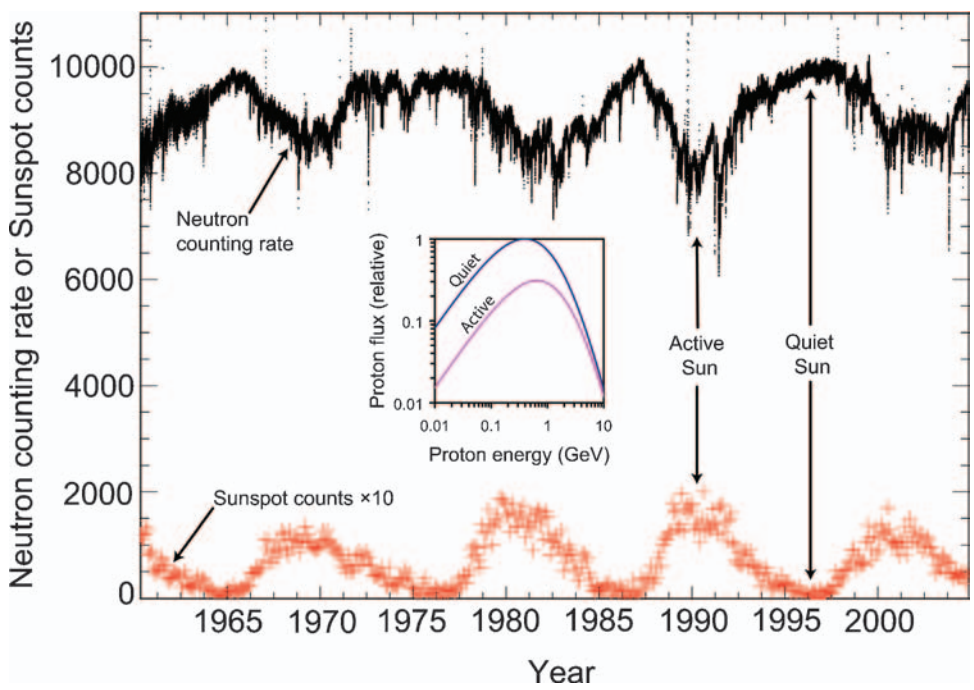

FIGURE 2 The variation of neutron counting rates (with units of hundreds of counts per hour) measured at McMurdo Station in Antarctica as a function of time (neutron monitors of the Bartol Research Institute are supported by NSF grant ATM-0000315). Monthly sunspot counts (multiplied by 10) are shown for comparison (Courtesy SIDC, RWC Belgium, World Data Center for the Sunspot Index, Royal Observatory of Belgium, 1961–2004). During periods of low solar activity (low sunspot counts), low energy galactic cosmic rays penetrate the heliosphere, which results in relatively high neutron production rates. During periods of high solar activity (high sunspot counts), the low energy galactic cosmic rays are cut off, resulting in lower neutron counting rates. The variation in neutron counting rates is about 20% over the solar cycle. Theoretical galactic proton energy spectra within the heliosphere, representative of quiet and active solar years, are shown (*inset*).

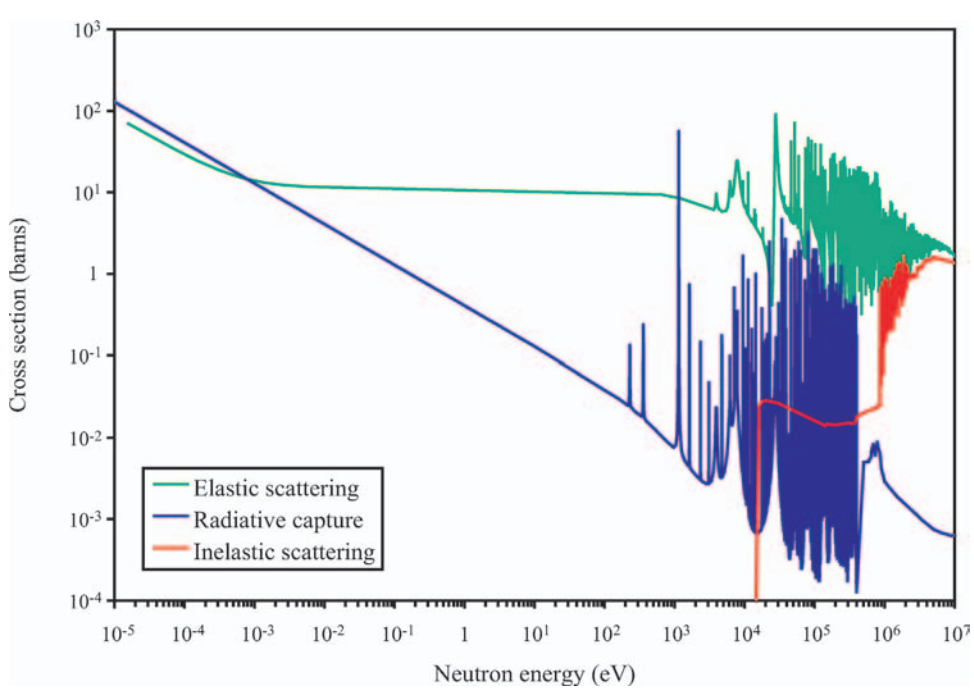

FIGURE 3 Neutron microscopic cross sections for natural Fe (*see text*).

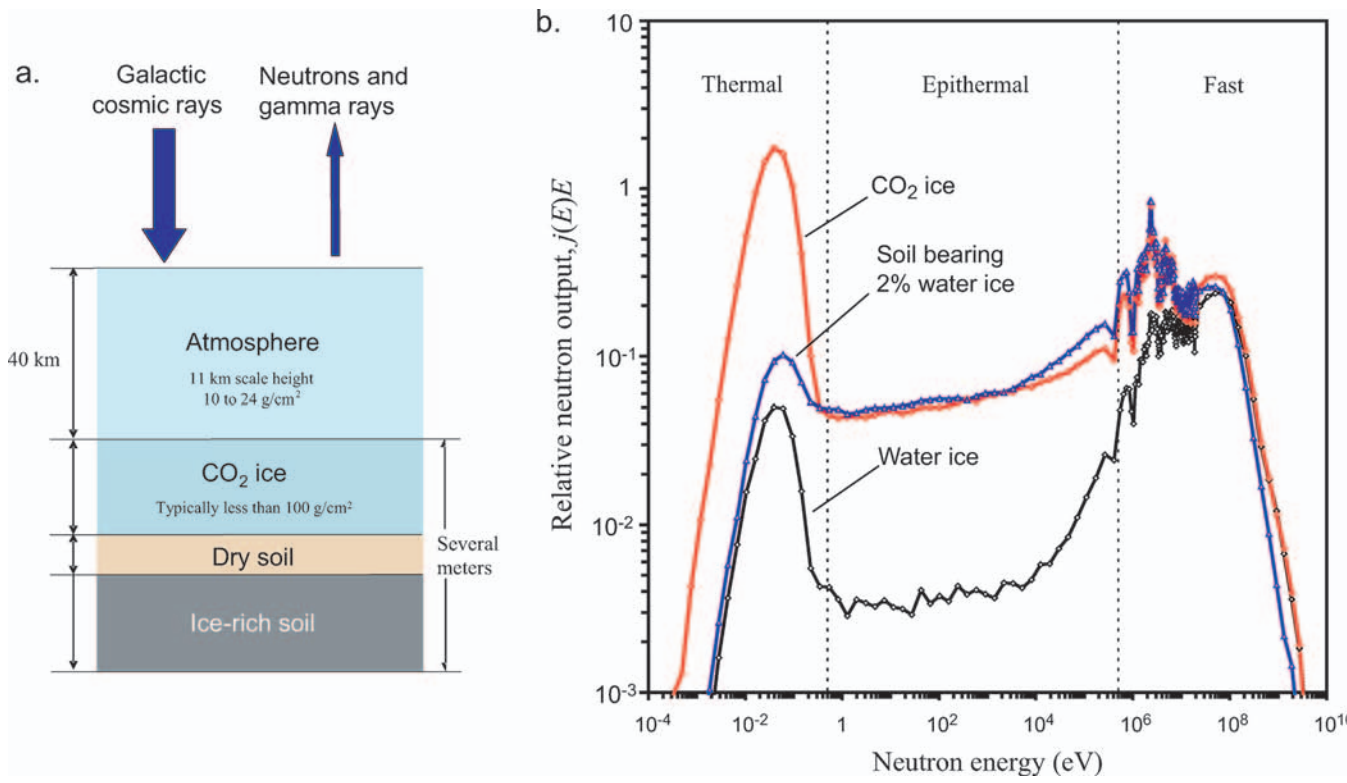

FIGURE 4 (a) Model of the martian surface at high latitudes; (b) The current of neutrons leaking away from Mars for three different solid surface compositions. Neutron energy ranges are indicated. (*See text for details.*)

Under the steady bombardment of cosmic rays, the population of neutrons slowing down in the surface is, on average, constant with time. The steady-state neutron energy-, angle-, and spatial-distributions depend on the composition and stratigraphy of the surface and atmosphere. An important property of the neutron population is the scalar flux (φ), which depends on depth and is given by the product of the speed of the neutrons, v (cm/s), and the number density of neutrons slowing down in the medium (n neutrons per cm^3): $\varphi = nv$, with units of neutrons per cm^2 per s. The rate at which neutrons interact with nuclei is given by the product of the flux of neutrons, the density of the target nuclei (N nuclei per cm^3), and the microscopic cross section: $R = \varphi N \sigma$ (interactions per cm^3 per s).

Cosmic ray showers can be modeled using Monte Carlo methods, in which the random processes of particle production and transport are simulated. The number of times something interesting happens, such as a particle crossing a surface, is tallied. Statistical averages of these interesting events are used to determine different aspects of the particle population such as fluxes and **currents**. Monte Carlo transport simulations generally provide for the following: a description of the cosmic ray source and the target medium (including geometry, composition, and density); detailed physical models of interaction mechanisms and transport processes (including tabulated data for interaction cross sections); and a system of tallies.

The general purpose code Monte Carlo N-Particle eXtended (MCNPX) developed by Los Alamos National Laboratory provides a detailed model of cosmic ray showers, including the intranuclear cascade and subsequent interactions of particles within the surface and atmosphere. For example, a model of the martian surface used to calculate neutron leakage spectra is shown in Fig. 4a, and includes several layers, representative of the high latitude surface, which is seasonally covered by CO_2 ice due to condensation of atmospheric CO_2 in the polar night, and whose frost-free surface consists of a dry lag deposit covering ice rich soil. The curvature of Mars was included in the MCNPX calculations along with details of the incident galactic proton energy distribution. The goal was to determine the effect of surface parameters on neutron output, including the **column abundance** (g/cm^2) of the layers, their water abundance, and major element composition. The variation of the density of the atmosphere with altitude (the scale height is roughly 11 km) and atmospheric mass were modeled. An accurate treatment of the atmosphere is needed in order to account for variations in neutron production with density by particles

such as pions that have very short half-lives. For dense atmospheres, these particles interact more frequently with atmospheric nuclei, resulting in increased neutron production in the atmosphere.

The population of neutrons escaping the surface or atmosphere can be represented as a current, J, which is the ratio of the number of neutrons escaping into space per galactic cosmic ray incident on the planet. The energy distribution of leakage neutrons is given by the current density $j(E)$, which is the number of escaping particles per unit energy per incident cosmic ray, such that $J = \int_0^\infty dE j(E)$. The current density of neutrons leaking away from Mars was calculated by MCNPX for homogeneous solid surfaces consisting of water ice, which is representative of the north polar residual cap; relatively dry soil bearing 2% water ice, which is representative of dry equatorial regions; and CO_2 ice, which is representative of the seasonal polar caps. The relative neutron output, given by the product of the current density and neutron energy is shown in Fig. 4b for each of these materials. Integrating over all energies gives 5, 3, and 1 for the total number of neutrons escaping the surface per incident cosmic ray proton for the CO_2 ice, dry soil, and water ice surfaces, respectively.

The neutron current density spans 14 decades of energy and can be divided into three broad ranges (Fig. 4b), representing different physical processes: (1) Thermal neutrons, which have undergone many collisions, have energies less than about 0.1 eV and are nearly in thermal equilibrium with the surface; (2) epithermal neutrons, which have energies greater than about 0.1 eV and are in the process of slowing down from higher energies; and (3) fast neutrons, including source neutrons and neutrons with energy greater than the threshold for inelastic scattering. Absorption and leakage result in a nonequilibrium energy distribution for the thermal spectrum. Consequently, the most probable neutron energy is slightly higher than would be predicted given the temperature of the surface.

Elastic scattering is the most important loss mechanism for planetary neutron spectroscopy because it provides strong differentiation between H and other more massive nuclei. For elastic scattering, the energy loss per collision varies systematically with atomic mass. The maximum energy that a neutron can lose in a collision is given by fE, where $f = 1 - [(A-1)/(A+1)]^2$, E is the energy of the neutron before the collision, and A is the atomic mass of the target nucleus. Thus, a neutron could lose all of its energy in a single collision with hydrogen ($A = 1$), which has roughly the same mass as a neutron. This fact is easily verified by observing head-on collisions in a game of billiards. In contrast, the maximum energy loss in a collision with C, which is the next most massive nucleus of interest in planetary science, is 28%. For Fe, the maximum energy loss per collision is 7%. The average energy loss per collision follows a similar trend. Consequently, for materials that are rich in H, such as water ice, energy loss by elastic collisions is high and neutrons slow down more quickly than for materials that do not contain H.

For H-rich materials, the population of neutrons that are slowing down is strongly suppressed relative to materials without H. For example, the epithermal current density for the simulated water ice surface in Fig. 4b is considerably lower than either the soil or CO_2 surfaces. The current density of fast neutrons, which have undergone relatively few collisions following their production, are influenced by elastic scattering, but also by variations in neutron production, which depend on the average atomic mass of the medium.

Absorption of neutrons by radiative capture significantly influences the population of thermal neutrons. Elements such as H, Cl, Fe, and Ti have relatively high absorption cross sections and can significantly suppress the thermal neutron flux. C and O have very low absorption cross sections compared to H. Consequently, the thermal neutron output for the water ice in Fig. 4b is suppressed relative to the surfaces containing CO_2 ice and soil.

2.3 Gamma Ray Production and Transport

For galactic cosmic ray interactions, gamma rays are primarily produced by neutron inelastic scattering and radiative capture. De-excitation of residual nuclei produced by these reactions results in the emission of gamma rays with discrete energies. The energies and intensities of the gamma rays provide a characteristic fingerprint that can be used to identify the residual nucleus. Since, in most cases, a residual nucleus can only be produced by a reaction with a specific target isotope, gamma rays provide direct information about the elemental composition of the surface.

For example, neutron inelastic scattering with ^{56}Fe frequently leaves the residual ^{56}Fe nucleus in its first excited state, which transitions promptly to ground state by the emission of an 847 keV gamma ray. The presence of a peak at 847 keV in a planetary gamma ray spectrum indicates that the surface contains Fe. The intensity of the peak is related directly to the abundance of elemental Fe in the surface.

Gamma rays produced by the decay of short-lived neutron activation products and long-lived (primordial) radioisotopes also provide useful information about elemental abundance. Radioactive elements such as K, Th, and U can be detected when present in trace quantities. Most notably, the Th decay chain produces a prominent gamma ray at 2.6 MeV, which can be measured when Th is present in the surface at low levels (>1 ppm).

To illustrate a typical gamma ray leakage spectrum, a Monte Carlo simulation of the lunar gamma ray leakage current induced by galactic cosmic ray protons is shown in Fig. 5. The composition of the surface was assumed to be the mean soil composition from the *Apollo 11* landing site. Contributions from nonelastic reactions and capture are plotted separately. A background component associated primarily

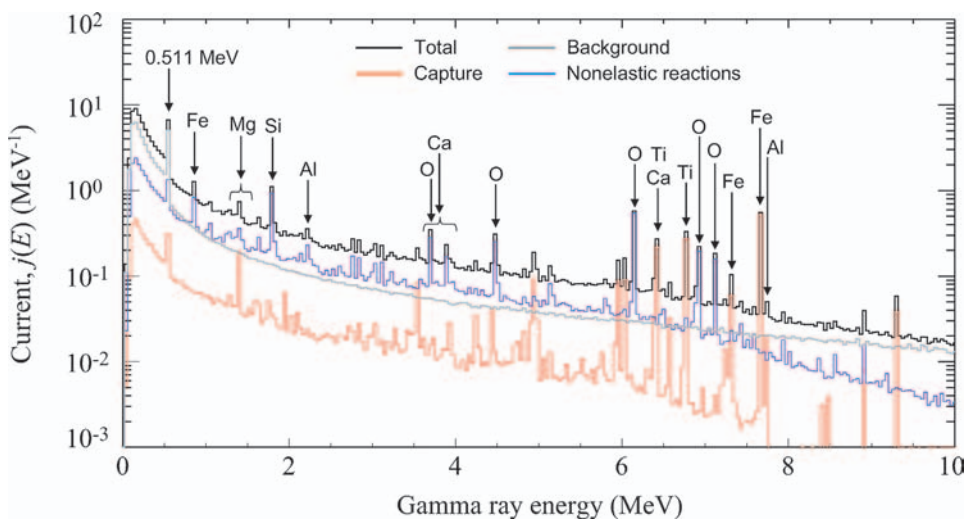

FIGURE 5 The current of gamma rays leaking away from the Moon for a composition representative of the *Apollo 11* landing site.

with the decay of pions is also shown. The peaks correspond to gamma rays that escape into space without interacting with the surface material. The peaks are superimposed on a continuum, which results from the scattering of gamma rays in the surface. The total number of gamma rays escaping the surface per incident cosmic ray proton was 2.7, which is within the range of values for the number of neutrons escaping the martian surface, presented in Section 2.1.

Gamma ray peaks associated with neutron interactions with major elements are labeled with the target element in Fig. 5. The intensity (or area) of each peak is proportional to the product of the abundance of the target element and the number density of neutrons slowing down in the medium. Specifically, the measured intensity (I) of a gamma ray peak with energy E for a selected reaction can be modeled as the product of three terms: $I \propto fyR$, where f accounts for attenuation of gamma rays by intervening surface materials and the variation of detection efficiency with gamma ray energy; y is the number of gamma rays of energy E produced per reaction; and $R = \varphi N \sigma$ is the **reaction rate**, the product of the neutron flux, cross section, and number density of the target element.

Because gamma rays are produced by neutron interactions, the absolute number density or, equivalently, the weight fraction of the target element cannot be determined unless the neutron flux is known. Thus, neutron spectroscopy plays an important role in the analysis of gamma ray data. Relative abundances can be determined without knowledge of the magnitude of the neutron flux. For example, the ratio of Fe to Si abundances can be determined from the ratio of the intensities of the prominent Fe doublet (at 7.65 MeV and 7.63 MeV) the Si gamma ray at 4.93 MeV. Because the magnitude of the attenuation of gamma rays by surface materials depends on gamma ray energy and the distribution of gamma ray production with depth, models of the depth profile of the neutron flux are needed in order to analyze gamma ray data.

For homogeneous surfaces, accurate results can be obtained for absolute and relative abundances; however, surfaces with strong stratigraphic variations present a difficult challenge for analyzing nuclear spectroscopy data. Compositional layering of major elements on a submeter scale is widespread on Mars as shown, for example, by the *Spirit* and *Opportunity* rovers [see Mars Site Geology and Geochemistry]. In some cases, geophysical assumptions can be made that simplify the analysis and allow quantitative results to be obtained; however, it is often the case that insufficient information is available. In these cases, it is sometimes possible to establish bounds on composition that are useful for geochemical analysis. Development of accurate algorithms for determining elemental abundances, absolute or relative, requires careful synthesis of nuclear physics with constraints from geology, geophysics, and geochemistry.

3. Detection of Gamma Rays and Neutrons

In this section, a simple model of the counting rate observed by orbiting neutron and gamma ray spectrometers is presented along with an overview of radiation detection concepts for planetary science applications.

3.1 Counting Rate Models

The flux of radiation reaching an orbiting spectrometer varies in proportion to the solid angle subtended by the planet at the detector, which depends on orbital altitude. The fractional solid angle of a spherical body is given by

$$\Omega(h) = 1 - \sqrt{1 - R^2/(R+h)^2}, \qquad (1)$$

where h is the orbital altitude and R is the radius. The fractional solid angle varies from 1 at the surface (for $h = 0$) to 0 far away from the planet. For galactic cosmic ray interactions, the flux of gamma rays or neutrons at the orbiting spectrometer is approximately

$$\phi(h) = 1/4\Phi J\,\Omega(h), \tag{2}$$

where Φ is the flux of galactic cosmic ray protons far from the planet (about 4 protons/cm^2/s, depending on the solar cycle and location within the heliosphere), and J is the leakage current. Because alpha particles and heavier nuclei of galactic origin contribute to neutron and gamma ray production, Eq. 2 must be multiplied by a factor, approximately 1.4, in order to estimate the total leakage flux.

Eq. 2 can be used, for example, to calculate the flux of neutrons incident on the *Mars Odyssey* neutron spectrometer. The orbital altitude for *Mars Odyssey* is 400 km, and the volumetric mean radius of Mars is 3390 km. The fractional solid angle, given by Eq. 1, is 0.55. The total leakage current for a surface consisting of thick CO_2 ice, representative of the polar seasonal caps during winter, was $J = 5$ (from Section 2.2). Consequently, from Eq. 2, the total flux of neutrons at *Odyssey's* orbit from thick CO_2 deposits is approximately 4 neutrons per cm^2 per s. For a surface that is 100% water, which is representative of the north polar residual cap, J was 1, and the total flux at orbital altitude is expected to be 0.8 neutrons per cm^2 per s.

Radiation detectors, such as the gamma ray and neutron spectrometers on *Mars Odyssey*, count particle interactions and bin them into energy or pulse-height spectra, for example, with units of counts per s per unit energy. For both gamma rays and neutrons, the net counting rate (with units of counts per s) for selected peaks in the spectrum is needed in order to determine elemental abundances.

The flux of particles (gamma rays or neutrons) incident on a spectrometer can be converted to counting rate (C), given the intrinsic efficiency (ε) and projected area (A) of the spectrometer in the direction of the incident particles:

$$C = \varphi(h)\,\varepsilon A. \tag{3}$$

The intrinsic efficiency is the probability that an incident particle will interact with the spectrometer to produce an event that is counted. Because particles can pass through the spectrometer without interacting, the intrinsic efficiency is always less than or equal to 1. For example, εA is on the order of 10 cm^2 for the *Mars Odyssey* epithermal neutron detector, which has a maximum projected area of about 100 cm^2. The efficiency-area product (εA) varies with the energy and angle of incidence of the particles. So, the value for εA used in Eq. 3 must be appropriately averaged over neutron energy and direction.

One of the main sources of uncertainty in measured counting rates is statistical fluctuations due to the random nature of the production, transport, and detection of radiation. While a detailed discussion of error-propagation is beyond the scope of this article, the most important result is given here: The statistical uncertainty (precision) in the counting rate is given by $\sigma = \sqrt{C/t}$, where t is the measurement time and C is the mean counting rate. For example, to achieve a precision of ($1\%\ \sigma/C = 0.01$) when $C =$ 10 counts per s, which is typical of the epithermal and thermal counting rates measured by the *Mars Odyssey* neutron spectrometer, a counting time of 1000 s is required. Longer counting times are needed when background contributions are subtracted, for example, to determine counting rates for peaks in gamma ray and neutron spectra. Uncertainties in the counting rate due to random fluctuations propagate to the uncertainties in elemental abundance and other parameters determined in the analysis of spectroscopy data. Long counting times are desired to minimize statistical contributions. Alternatively, improved precision can be achieved by increasing the counting rate, which can be accomplished through instrument design, by maximizing, and/or by making measurements at low altitude.

3.2 Gamma Ray and Neutron Detection

Radiation spectrometers measure ionization produced by the interaction of particles within a sensitive volume. Gamma ray interactions produce swift primary electrons that cause ionization as they slow down in the sensitive volume. Neutrons undergo reactions that produce energetic ions and gamma rays. The recoil proton from neutron elastic scattering with hydrogen can produce measurable ionization. The charge liberated by these interactions can be measured using a wide variety of techniques, two of which are illustrated here.

Semiconductor radiation detectors typically consist of a semiconductor dielectric material sandwiched between two electrodes. An electric field is established in the dielectric by applying high voltage across the electrodes. Gamma ray interactions produce free electron-hole pairs which drift in opposite directions in the electric field. As they drift, they induce charge on the electrodes, which is measured using a charge-sensitive preamplifier. The amplitude of the charge pulse, or pulse-height, is proportional to the energy deposited by the gamma ray. Consequently, a histogram of pulse heights, known as a pulse-height spectrum, measured for many interactions provides information about the energy distribution of the incident gamma rays.

For example, a diagram of a high-purity germanium (HPGe) detector is shown in Fig. 6a along with a photograph of an HPGe crystal in Fig. 6b. The closed-end coaxial geometry is designed to minimize trapping of carriers as they drift to the electrodes. To minimize noise due to leakage current, the HPGe must be operated at very low temperatures. The requirement for cooling adds to the mass and complexity of the design for space applications.

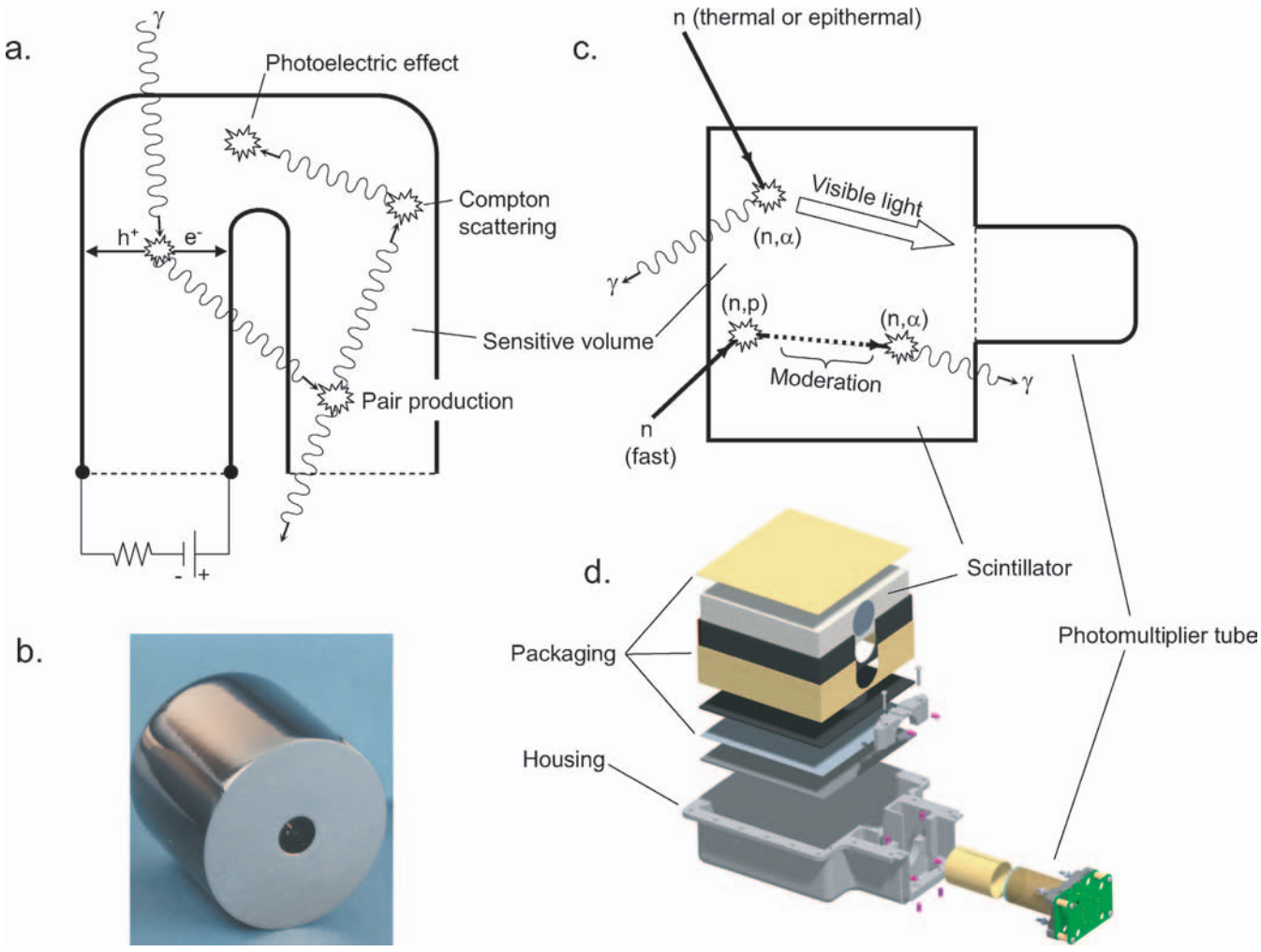

FIGURE 6 (a) Schematic diagram of a coaxial HPGe spectrometer and gamma ray interactions; (b) photograph of a HPGe cystal; (c) diagram of a scintillation-based spectrometer with neutron interactions; and (d) assembly diagram for a boron-loaded plastic scintillator for a flight experiment, including the mechanical structure (including packaging designed to withstand the vibrational environment during launch). (Part b courtesy of AMETEK, Advanced Measurement Technology, Inc., ORTEC Product Line, 801 South Illinois Avenue, Oak Ridge, TN 37830).

A hypothetical gamma ray interaction is superimposed on the diagram in Fig. 6a. Gamma rays undergo three types of interactions: pair production, Compton scattering, and the photoelectric effect. High-energy gamma rays (greater than 1.022 MeV) can undergo pair production, in which the gamma ray disappears and an electron-positron pair is produced. The kinetic energy of the electron and positron is absorbed by the medium. When the positron is annihilated by an electron, two, back-to-back (511 keV) gamma rays are produced, which can undergo additional interactions. In Compton scattering, a portion of the energy of the gamma ray is transferred to an electron. The energy lost by the gamma ray depends on the scattering angle. At low energies, the gamma ray can be absorbed by an electron via the photoelectric effect. All of these interactions vary strongly with the atomic number (Z) and density of the detector material. High Z, high density and a large sensitive volume is desired to maximize the probability that all of the energy of the incident gamma ray is absorbed in the detector.

A pulse height spectrum for a large volume (slightly larger than the crystal flown on *Mars Odyssey*), coaxial HPGe detector is shown in Fig. 7. The gamma rays were produced by moderated neutrons, with an energy distribution similar to the lunar leakage spectrum, incident on an Fe slab. Well-defined peaks corresponding to neutron capture and inelastic scattering with Fe appear in the spectrum. For example, the doublet labeled Fe(1) corresponds to gamma

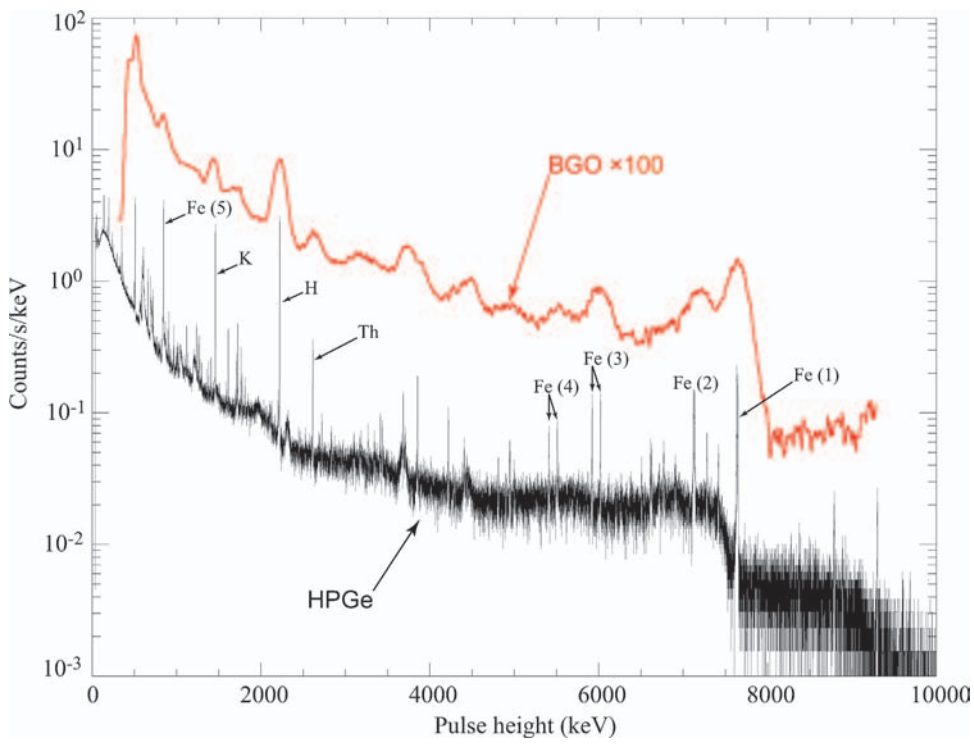

FIGURE 7 Gamma ray spectra acquired by HPGe (black) and BGO (red) spectrometers. To improve visualization, the spectrum for BGO has been multiplied by 100. The source was moderated neutrons, with energy distribution similar to a planetary leakage spectrum, incident on an iron slab. Gamma rays from natural radioactivity in the environment are also visible (from K at 1461 keV and Th at 2615 keV). A gamma ray at 2223 keV from neutron capture with H (from polyethylene in the moderator) is a prominent feature in the HPGe and BGO spectra. Major gamma rays from neutron interactions with Fe that are resolved by the HPGe spectrometer are labeled: (1) 7646- and 7631-keV doublet from neutron capture; (2) their single escape peaks; (3) 6019- and 5921-keV gamma rays from neutron capture; (4) their single escape peaks; and (5) 846.7 keV gamma ray from neutron inelastic scattering. (HPGe spectrum courtesy of S. Garner, J. Shergur, and D. Mercer of Los Alamos National Laboratory).

rays (7646- and 7631-keV) produced by neutron capture with Fe. The peaks labeled Fe(2) are shifted 511 keV lower in energy and correspond to the escape of one of the 511 keV gamma rays produced by pair production in the spectrometer. The continuum that underlies the peaks is caused by external Compton scattering and the escape of gamma rays that scattered in the spectrometer. Gamma rays from neutron capture with H and the radioactive decay of K and Th are also visible.

Scintillators provide an alternative method of detecting ionizing radiation, which can be used for gamma ray and neutron spectroscopy. Scintillators consist of a transparent material that emits detectable light when ionized. The light is measured by a photomultiplier tube or photodiode, which is optically coupled to the scintillator. The amount of light produced and the amplitude of the corresponding charge pulse from the photomultiplier tube and pulse processing circuit is proportional to the energy deposited by the radiation interaction.

A diagram of a boron-loaded, plastic scintillation detector is shown in Fig. 6c along with an assembly diagram of flight sensor (Fig. 6d). Thermal and epithermal neutrons are detected by the $^{10}B(n,\alpha\gamma)^{7}Li$ reaction. The recoiling reaction products (alpha particle and ^{7}Li ion) produce ionization equivalent to a 93 keV electron, which makes a well-defined peak in the pulse height spectrum. The area of the peak depends on the flux of incident thermal and epithermal neutrons. Thermal neutrons can be filtered out by wrapping the scintillator in a Cd foil, which strongly absorbs neutrons with energies below about 0.5 eV. Thus, the combination of a bare and Cd-covered scintillator can be used to separately measure contributions from thermal and epithermal neutrons. Above about 500 keV, light is produced by recoiling protons from neutron elastic scattering with hydrogen in the scintillator. Fast neutrons (greater than about 500 keV) can be detected by a prompt pulse from proton recoils followed a short time later by a second pulse, corresponding to neutron capture of the moderated neutron by

^{10}B. This characteristic, double-pulse time signature can be used to identify, and separately measure, fast neutron events.

Scintillators are also used routinely for gamma ray spectroscopy. For example, a pulse height spectrum acquired by a bismuth germanate (BGO) scintillator is shown in Fig. 7. The source was exactly the same as measured by the HPGe spectrometer, and the two spectra share similar peak features. Note, however, that the peaks measured by BGO are considerably broader than those measured by HPGe. The width of the peaks is caused by statistical variations in the number of scintillation photons produced in the BGO. Similar dispersion occurs for charge carriers (electrons and holes) in the HPGe crystal; however, the effect is far less pronounced. The pulse height resolution as measured by the full-width-at-half-maximum (FWHM) of the gamma ray peaks is much worse for the BGO than the HPGe. The ability of the HPGe technology to resolve individual peaks is coveted by the planetary spectroscopist; however, the added cost and complexity of HPGe relative to scintillation technology has made scintillators competitive for some missions.

Other technologies that have been flown for gamma ray and neutron detection include ^{3}He ionization chambers (for thermal and epithermal neutron detection on *Lunar Prospector*) and various scintillators, including Tl-doped NaI on NEAR and *Apollo* and Tl-doped CsI on *Phobos*. The *Dawn* mission will fly a new compound semiconductor technology (CdZnTe), which has significantly improved pulse height resolution relative to BGO and, in contrast to HPGe, can be operated at ambient temperatures.

3.3 Spatial Resolution

The spatial resolution that can be achieved by a spectrometer depends on the angular distribution of radiation emitted from the surface, the angular response of the spectrometer, and the altitude of the orbit. The angular response of most spectrometers is roughly isotropic or weakly dependent on incident direction. Consequently, the spectrometer is sensitive to radiation emitted from locations from underneath the spectrometer all the way out to the limb. Due to their increased area, off-nadir regions contribute more to the counting rate than regions directly beneath the spacecraft.

When the spectrometer passes over a point source of radiation on the surface, the counting rate as a function of distance along the orbital path has an approximately Gaussian shape, with the peak occurring when the spacecraft passes over the source. Consequently, the ability of the spectrometer to resolve spatial regions with different compositions depends on the FWHM of the Gaussian, which as a rule of thumb is approximately 1.5 times the orbital altitude. For example, the lowest orbital altitude of *Lunar Prospector* was 30 km for which the spatial resolution was 45 km or 1.5° of arc length. For *Mars Odyssey*, the orbital altitude was 400 km, and the spatial resolution was approximately 600 km or 10° of arc length.

The broad spatial response of gamma ray and neutron spectrometers must be considered in the analysis and interpretation of data, especially where comparisons to high-resolution data (for example, from optical spectroscopy) are concerned. It may be possible to increase the resolution of a spectrometer by the addition of a collimator, which would add mass to the instrument and also reduce the precision of the measurements. Alternatively, spatial deconvolution and instrument modeling techniques can sometimes be employed to study regions that are smaller in scale than the spatial resolution of the spectrometer.

4. Missions

Since the dawn of space flight, nuclear spectroscopy has been used for a wide variety of applications, from astrophysics to solar astronomy. Orbital planetary science missions with gamma ray and/or neutron spectrometers on the payload are listed in Table 1. While nuclear spectroscopy was used on earlier missions to the Moon, Mars, and the surface of Venus, the first major success was the Apollo Gamma Ray Experiment, which flew on the *Apollo 15* and *16* missions, providing global context for lunar samples. *Phobos II* traveled to Mars and provided a glimpse of the regional composition of the western hemisphere, which includes Tharsis and Valles Marineris. Due to the small size of Eros and high orbital altitudes, the gamma ray spectrometer on *NEAR* provided little useful information about Eros until the *NEAR* landed on the asteroid. Once on the surface, the *NEAR* gamma ray spectrometer acquired data with sufficient precision to determine the abundance of O, Mg, Si, Fe, and K. *NEAR* also had an x-ray spectrometer that provided complementary information about surface elemental composition. The first intended use of neutron spectroscopy for global mapping was on *Mars Observer*, which was lost before reaching Mars.

Lunar Prospector was the first mission to combine gamma ray and neutron spectroscopy to provide accurate, high-precision global composition maps of a planetary body. The missions that followed *Lunar Prospector*, including *2001 Mars Odyssey* and *MESSENGER*, a mission to the planet Mercury, also included neutron and gamma ray spectrometers on the payload. *Dawn*, a mission to the main asteroid belt, and *Selene*, a lunar mission, represent the future of orbital planetary spectroscopy. Both are in preparation for launch in the 2006–2007 timeframe.

5. Science

Lunar Prospector and *Mars Odyssey* acquired high-precision gamma ray and neutron data sets for the Moon and

TABLE 1 Summary of orbital planetary science and exploration missions with gamma ray and/or neutron spectrometers. Missions prior to Apollo, including Luna and Ranger, are not listed.

Mission	Country/ Program	Launch date(s)	Status	Planet or minor body	Orbit	Mapping duration[a]	Gamma ray spectrometer	Neutron spectrometer	Results or Objectives[b]
Apollo 15 and 16	U.S.	26-Jul-1971 16-Apr-1972	Completed	Moon	Equatorial orbit covering 20% of the lunar surface	10.5 days (Apollo 15 and 16 combined)	NaI(Tl) with plastic anti-coincidence shield	None	Maps of major and radioactive elements, including Fe, Th, and Ti.
Phobos II[c]	U.S.S.R.	12-July-1988	Lost during Phobos encounter	Mars and Phobos	Elliptical, equatorial orbit, 900 km periapsis, 80,000 km apoapsis	2 orbits analyzed	CsI(Tl)	None	Abundances for O, Si, Fe, K and Th in two equatorial regions in the western hemisphere
Mars Observer	U.S., NASA Mars Exploration Program	25-Sep-1992	Lost prior to orbital insertion	Mars	400 km altitude circular polar mapping orbit[b]	1 Mars year[b]	HPGe, passively cooled	Boron-loaded plastic scintillators	Global maps major elements and water-equivelent hydrogen (Objectives not achieved)
Near Earth Asteroid Rendezvous (NEAR)	U.S., NASA Discovery Program	17-Feb-1996	Completed mission	Eros	Useful data acquired following successful landing on Eros	7 days on the surface	NaI(Tl) with BGO antico-incidence shield	None	Abundances for O, Mg, Si, Fe, and K
Lunar Prospector	U.S., NASA Discovery Program	6-Jan-1998	Completed mission by planned impact in a south polar crater	Moon	High and low altitude circular polar mapping orbits (100 km and 30 km, respectively)	300 days at high altitude; 220 days at low altitude	BGO with boron-loaded plastic anti-coincidence shield	^{3}He gas proportional counters and boron-loaded plastic scintillator	Discovery of enhanced water-equivalent hydrogen associated with polar cold traps; global maps of major and radioactive elements

2001 Mars Odyssey	U.S., NASA Mars Exploration Program	7-Apr-2001	Completed primary mission; extended mission underway	Mars	400 km altitude circular polar mapping orbit	Over 2 Mars years completed, Extended mission in progress	HPGe, passively cooled	Boron-loaded plastic scintillators (NS); Stilbene and ^{3}He tubes (HEND[d])	Distribution of water-equivalent hydrogen and high-latitude stratigraphy; seasonal variations in CO_2 ice and noncondensable gasses; and global maps of major and radioactive elements
MESSENGER	U.S., NASA Discovery Program	3-Aug-2004	Cruise phase	Mercury	Elliptical polar orbit with periapsis at 200 km altitude, 60°N latitude, 15,000 km apoapsis[b]	1 year starting in 2011[b]	HPGe, actively cooled	^{6}Li-loaded glass and boron-loaded plastic scintillators	Maps of elemental composition in the northern hemisphere; search for polar hydrogen deposits
Dawn	U.S., NASA Discovery Program	Summer, 2007	Perparing for launch[e]	Vesta and Ceres	Survey, high, and low altitude circular polar mapping orbits[b]	6 months at each asteroid[b]	CdZnTe and BGO	^{6}Li-loaded glass and boron-loaded plastic scintillators	Global maps of major and radioactive elements and ice constituents (H and C)
Selene	Japan	2007, TBD	Preparing for launch[e]	Moon	100 km circular polar mapping orbit	1 year	HPGe, actively cooled	None	Abundance of major and radioactive elements.

[a]Refers to the time periods during which gamma ray and/or neutron data were acquired.
[b]Objectives are listed for Mars Observer, MESSENGER, Dawn, and Selene.
[c]Neutron and gamma ray spectrometers were flown on Phobos I, which was launched on 7-July-1988; however, Phobos I was lost during the cruise phase of the mission. The Mars 4 and 5 missions (U.S.S.R., 1973) flew identical sodium iodide gamma ray spectrometers. A few gamma ray spectra were acquired by Mars 5 while in an elliptical orbit around Mars (apoapsis 32,560 km, periapsis 1760 km, inclination 35° to the equator).
[d]The high energy neutron detector (HEND) was provided by the Russian Federation.
[e]Future missions that have advanced past the planning stage are listed.

Mars, respectively. Highlights of the science carried out on these missions are presented along with a description of their instrumentation. The Moon and Mars are very different, both in their origin and composition. With the possible exception of polar water ice, the Moon is bone dry and has no atmosphere. The lunar surface has been extensively modified by cratering and basaltic volcanism. Mars has a tenuous atmosphere, extensive water ice deposits, and seasonal CO_2 caps. Volcanic, aqueous, and eolian processes have continued to shape the surface of Mars long past the primordial formation of the crust. The differences between these two bodies will provide the reader with insights into the wealth of information provided by nuclear spectroscopy and the challenges faced in the analysis of the data. For *Lunar Prospector*, emphasis is placed on the combined analysis of neutron and gamma ray data to determine the abundance of major and trace radioactive elements. For *Mars Odyssey*, results from the neutron spectrometer for global water abundance and the seasonal caps are presented.

5.1 Lunar Prospector

Lunar Prospector was a spin-stabilized spacecraft, with the spin axis perpendicular to the plane of the ecliptic. The instruments were deployed on booms to minimize backgrounds from the spacecraft (Fig. 8a). The payload included a large-volume BGO gamma ray spectrometer (GRS), which was surrounded by a boron-loaded plastic anticoincidence shield (Fig. 8b). The shield served two purposes: (1) to suppress the Compton continuum caused by gamma rays escaping the BGO crystal and to reject energetic particle events; and (2) to measure the spectrum of fast neutrons from the lunar surface using the double-pulse technique described in Section 3.2. Sn- and Cd-covered ^{3}He gas proportional counters were used to detect and separately measure thermal and epithermal neutrons. Gamma ray and neutron spectroscopy data were acquired for long periods of time (Table 1), providing full coverage of the Moon at 100- and 30-km altitude.

The data were analyzed to determine global maps of surface elemental composition. The resulting abundance data were mapped on different spatial scales, depending on the precision of the data and the altitude of the spectrometer. Results of the analysis were submitted to the NASA Planetary Data System and include the following data sets: the abundance of hydrogen from neutron spectroscopy (0.5° **equal angle map**); the average atomic mass from fast neutron spectroscopy (2° **equal area maps**); the abundance of major oxides, including MgO, Al_2O_3, SiO_2, CaO, TiO_2, and FeO, and trace incompatible elements K, Th, and U

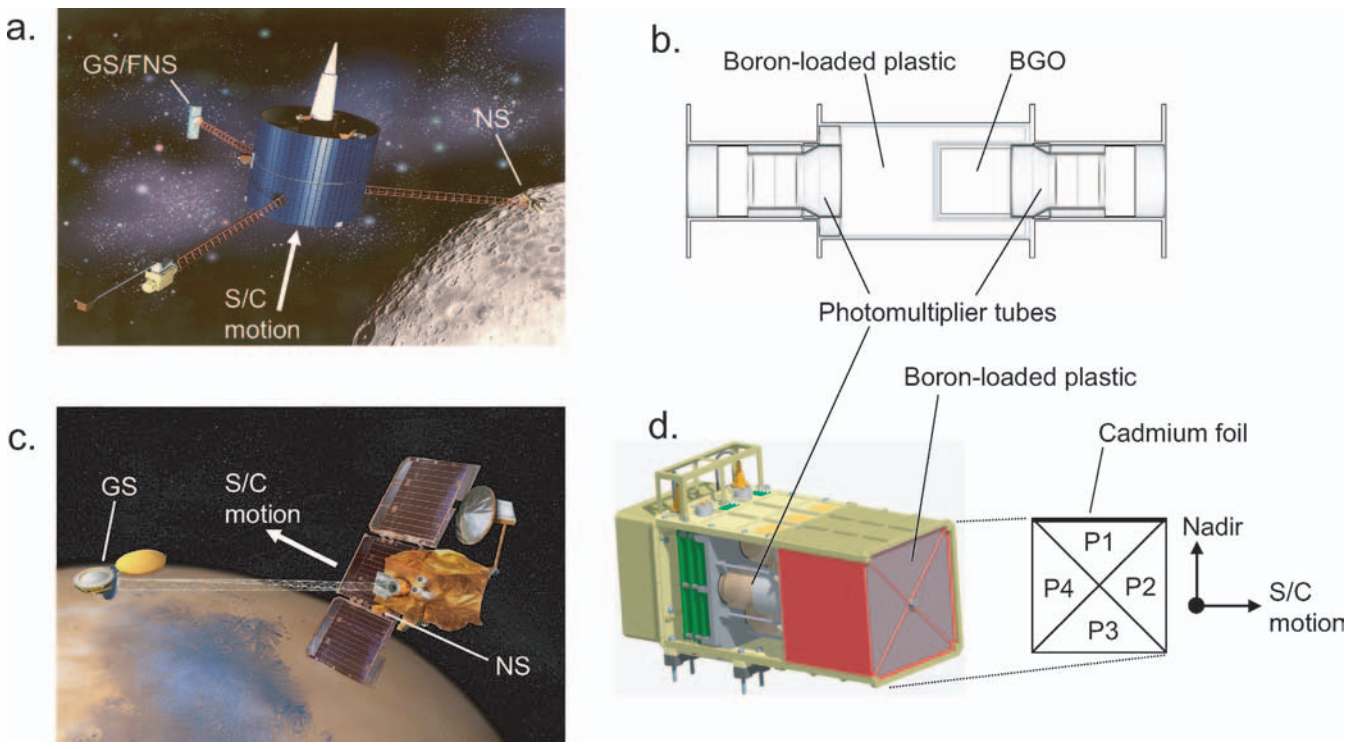

FIGURE 8 (a) Annotated artist's conception of *Lunar Prospector*; (b) Cross sectional view of the gamma ray and fast neutron spectrometer; (c) annotated artist's conception of *2001 Mars Odyssey*; (d) engineering drawing of the Neutron Spectrometer on *Odyssey* cut-away to show the boron loaded plastic scintillators. A schematic diagram of the arrangement of scintillators and their orientation relative to spacecraft motion and nadir is also shown. (Parts a and c courtesy of NASA.)

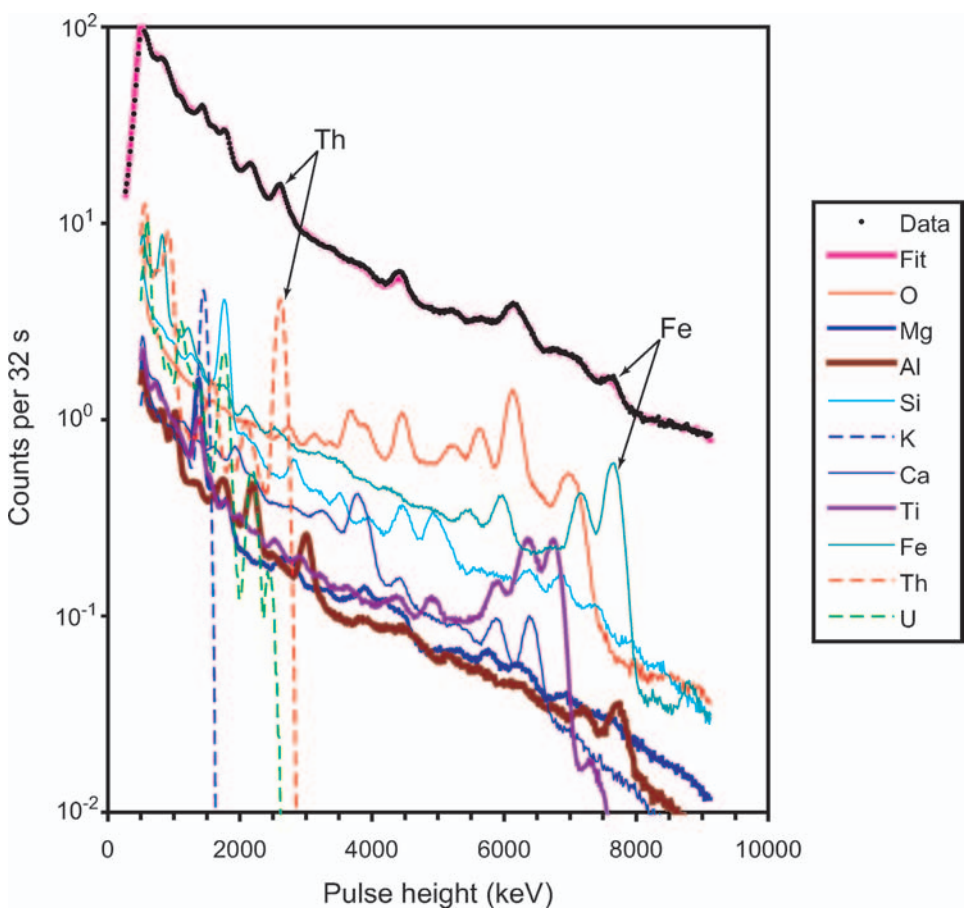

FIGURE 9 *Lunar Prospector* gamma ray spectrum for a 20° equal-area pixel in the western mare is compared to the fitted spectrum and elemental spectral components (*see text for details*).

(2°-, 5°-, and 20°-equal area maps) using a combination of gamma ray and neutron spectroscopy; and the abundance of the rare-earth elements (Gd + Sm) from neutron spectroscopy (0.5° equal angle map).

Perhaps the most significant result of *Lunar Prospector* was the discovery of enhanced hydrogen at the poles in association with craters in permanent shadow, which are thought to be cold traps for water ice. If present, water ice could be an important resource for manned exploration. Consequently, the polar cold traps are a prime target for future missions. Geochemical results from the analysis of neutron and gamma ray spectra fully reveal the dichotomy in the composition of the Moon, with a near side that is enriched in incompatible elements and mafic minerals and a thick far-side crust primarily consisting of plagioclase feldspar.

Global geochemical trends observed by *Lunar Prospector* are not significantly different from trends observed in the sample and meteoritic data; however, there are some notable discrepancies that point to the existence of unique lithologies that are not well represented by the lunar sample data. Interpretation and analysis of the data is ongoing with emphasis on regional studies. For example, the impact that formed the South Pole Aitken (SPA) basin could have excavated into the mantle. Analysis of the composition of the basin floor may reveal information about the bulk composition of the mantle and lower crust.

The analysis of major and radioactive elements was carried out using a combination of gamma ray and neutron spectroscopy data. A typical gamma ray spectrum is shown in Fig. 9 for a 20° equal-area pixel in the western mare. Two intense, well-resolved peaks, labeled in Fig. 9, were analyzed to determine the abundance of Fe and Th. In addition, a spectral unmixing algorithm similar to those used to analyze spectral reflectance data was developed to simultaneously determine the abundance of all major and radioactive elements from the gamma ray spectrum.

Lunar gamma ray spectra can be modeled as a linear mixture of elemental spectral shapes. The magnitude of the spectral components must be adjusted to account for the nonlinear coupling of gamma ray production to the neutron number density (for neutron capture reactions) and the flux of fast neutrons (for nonelastic reactions). Once the adjustment is made, a linear least squares problem can be solved to determine elemental weight fractions. Fitted elemental spectral shapes are shown, for example, in Fig. 9.

Abundance maps for selected elements determined by *Lunar Prospector* are shown in Fig. 10. To provide context for the elemental abundance maps, a map of topography determined by *Clementine*, superimposed on a shaded

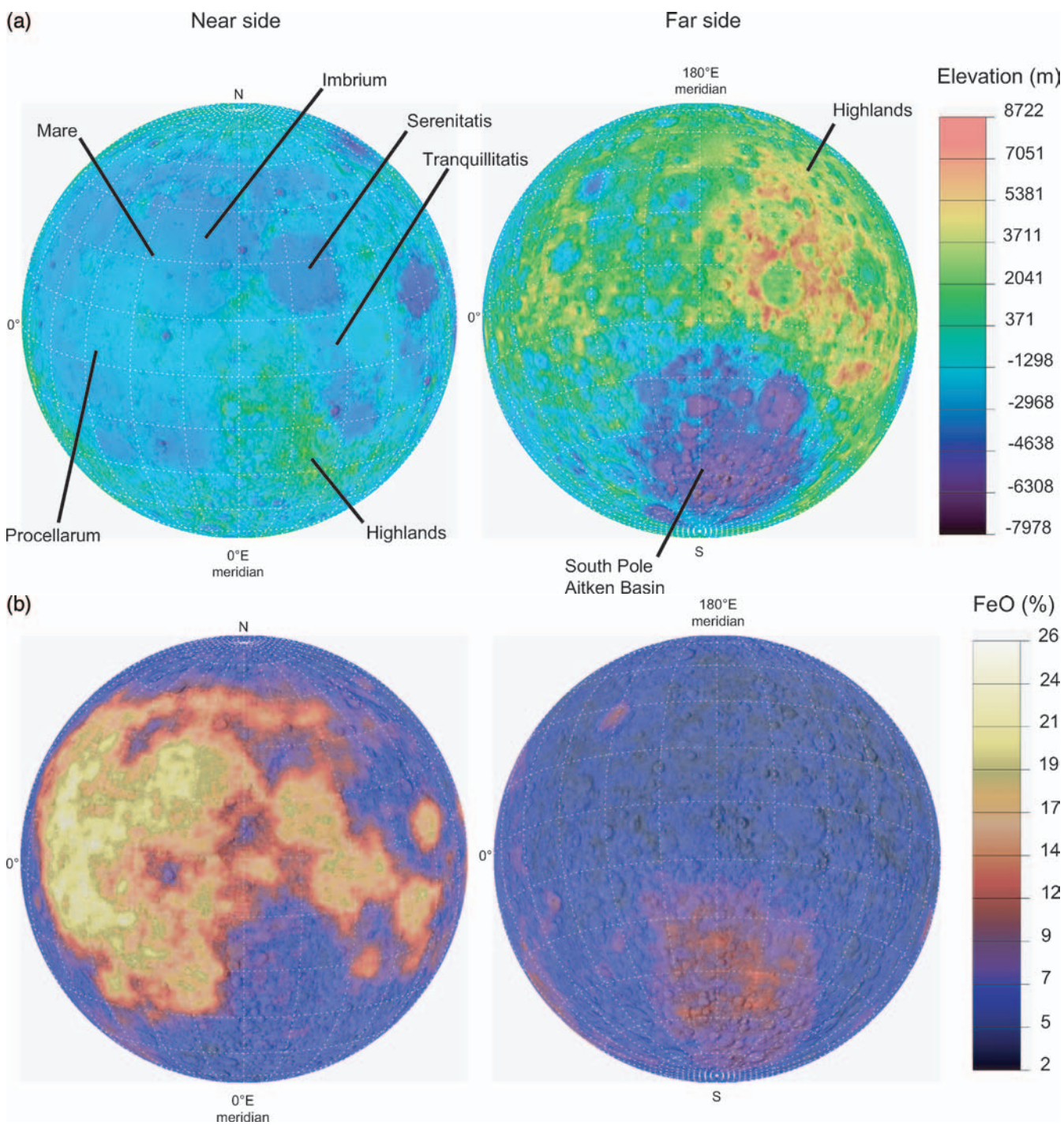

FIGURE 10 Orthographic projections of the lunar near and far sides: (a) Elevation; (b–d) abundance (weight fraction) of selected elements. The map data are superimposed on a shaded relief image. (FeO data courtesy NASA Planetary Data System ; image courtesy United States Geological Survey.)

relief image, is shown in Fig. 10a. The far side includes the feldspathic highlands and the SPA basin. The near side consists of major basins, including Procellarum and Imbrium, which contain mare basalts. The mare basalts are rich in Fe, with the highest concentrations occurring in western Procellarum (Fig. 10b). The low abundance of FeO in the highlands, which are rich in plagioclase feldspar, reflects a significant lunar geochemical trend in which mafic silicate minerals are displaced by plagioclase, which is Fe-poor.

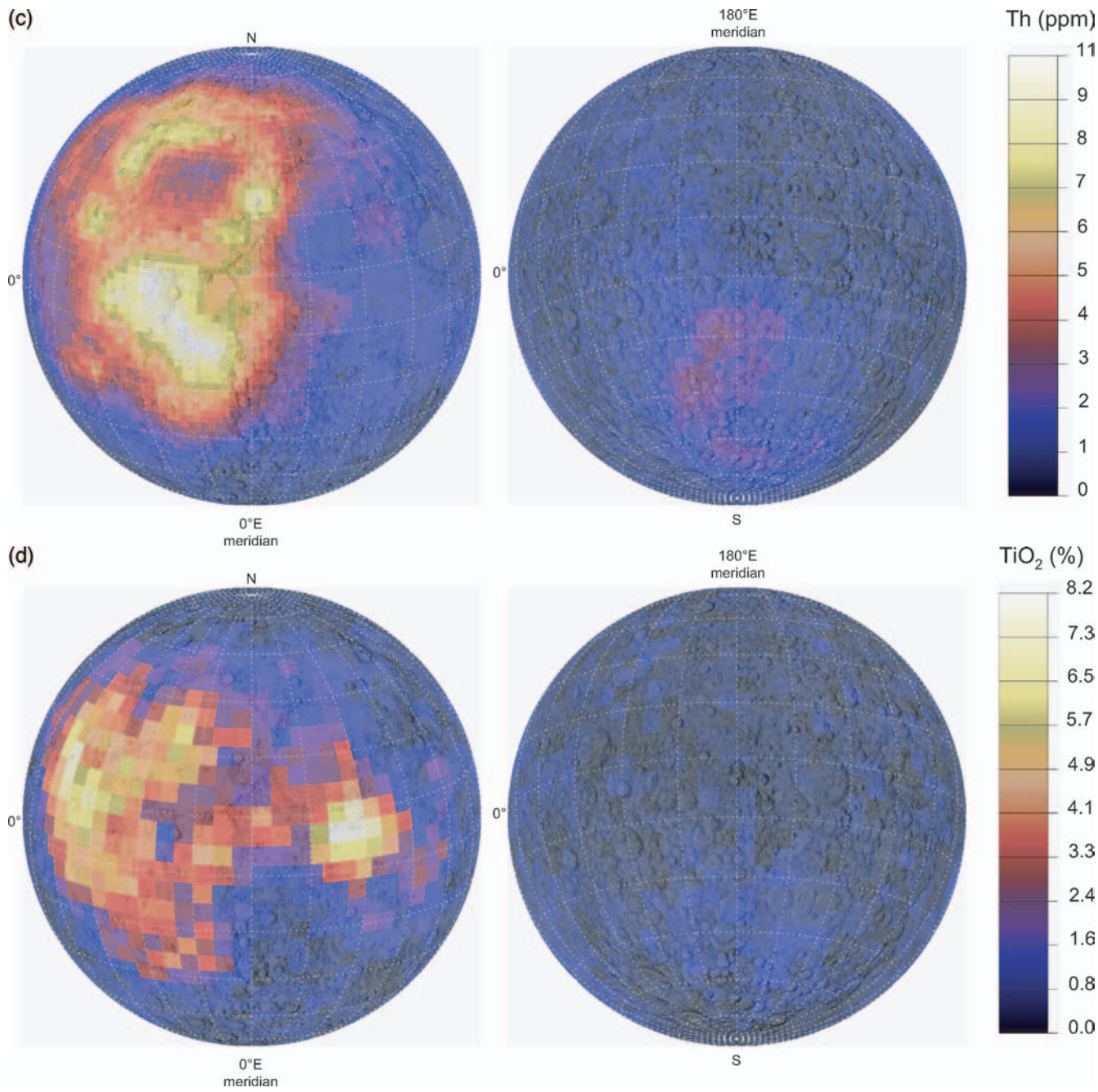

FIGURE 10 (*Continued*)

A large portion of the western near side is enriched in radioactive elements such as Th (Fig. 10c). K, Th, and U are incompatible with major lunar minerals and were likely concentrated in the residual melt during lunar differentiation. Consequently, their distribution on the surface and with depth has important implications to lunar evolution. The association of high Th concentrations with the mare suggests that heating by radioactive elements may have significantly influenced lunar thermal evolution and mare volcanism.

The distribution of TiO_2 is shown in Fig. 10d as a 5° equal area map. The low spatial resolution of the TiO_2 map compared to FeO and Th is a consequence of the relatively low intensity of the Ti gamma rays and their position in the gamma ray spectrum near strong peaks from O and Fe (Fig. 9). The abundance of TiO_2 can be used to classify mare basalts. Strong spatial variations in the abundance of TiO_2, for example, indicate that different source regions and processes were involved in creating the basalts

that comprise the mare. The highest concentrations of TiO_2 are found in Tranquillitatis as shown in Fig. 10d; however, high concentrations are also found in western Procellarum. The abundances of Fe and Ti observed in western Procellarum suggest that this region has a unique composition that is not well represented by the lunar samples.

5.2 Mars Odyssey

As of this writing, *2001 Mars Odyssey* is in an extended mission having successfully completed over two Mars years of mapping (each Mars year is 687 days). *Odyssey* is in a circular polar mapping orbit around Mars at an altitude of approximately 400 km (Table 1). The nuclear spectroscopy payload consists of a GRS, a neutron spectrometer (NS), and a Russian-supplied high energy neutron detector (HEND). Gamma ray and neutron spectroscopy data acquired by *Mars Odyssey* provide constraints on geochemistry, the water cycle, climate history, and atmospheric processes, including atmospheric dynamics and atmosphere-surface interactions [see Mars Atmosphere: History and Surface Interaction].

Since the discovery of abundant subsurface **water-equivalent hydrogen** (WEH) at high latitudes, *Odyssey's* gamma ray and neutron spectrometers have continued to provide a wealth of new information about Mars, including the global distribution of near-surface WEH, the elemental composition of the surface, seasonal variations in the composition of the atmosphere at high latitudes, and the column abundance of CO_2 ice in the seasonal caps. This information has contributed to our understanding of the recent history of Mars: The climate is driven strongly by short-term variations in orbital parameters, principally the obliquity, and the surface distribution of surface water-ice is controlled by atmosphere-surface interactions. The discovery of anomalously large amounts of WEH at low latitudes, where water ice is not stable, has stirred considerable debate about the mineral composition of the surface and climate change.

The GRS on *Odyssey* is boom-mounted, passively cooled, HPGe spectrometer, similar in design to the instrument flown on *Mars Observer* (Fig. 8c). The NS is a deck-mounted instrument that consists of a boron-loaded plastic block (roughly 10 cm on a side), which has been diagonally segmented into four prisms and read out by separate photomultiplier tubes (Fig. 8d). The orientation of the spacecraft is constant such that one of the prisms faces nadir (P1), one faces zenith (P3), one faces in the direction of spacecraft motion (P2), and one faces opposite the spacecraft motion (P4). P1 is covered with a Cd foil that prevents thermal neutrons from entering the prism. Consequently, P1 is sensitive to epithermal and fast neutrons originating from the surface and atmosphere.

Neutrons with energy less than the gravitational binding energy of Mars, approximately 0.13 eV, corresponding to an escape speed of about 5000 m/s, travel on parabolic trajectories and return to Mars unless they decay by beta emission. The mean lifetime of a neutron is approximately 900 s. The most probable energy for neutrons in thermal equilibrium with the surface of Mars (for the mean martian temperature of 210 K) is 0.018 eV, which corresponds to a neutron speed of 1860 m/s. Consequently, a significant portion of the thermal neutron population travels on ballistic trajectories and are incident on the spectrometer from above and below. Neutrons that leave the atmosphere with energies less than about 0.014 eV, just below the most probable energy, cannot reach the 400 km orbital altitude of *Odyssey*. Consequently, gravitational binding has a significant effect on the flux and energy distribution of neutrons at *Odyssey's* orbital altitude, and, in contrast to the simplified discussion in Section 3.1, gravitational effects must be accounted for in models of the flux and instrument response.

To separate thermal and epithermal neutrons, the NS makes use of the orbital speed of the spacecraft, which is approximately 3400 m/s, the same speed as a 0.05 eV neutron. Neutrons below the speed of the spacecraft (most of the thermal neutron population) can't catch up to P4. So, P4 is primarily sensitive to epithermal neutrons. In contrast, P2 "rams" into thermal neutrons that arrive at the orbital altitude ahead of the spacecraft. P2 has roughly the same sensitivity as P4 for epithermal neutrons. Consequently, the thermal flux is given by the difference between the counting rates for P2 and P4.

Thermal, epithermal, and fast neutrons are sensitive to surface and atmospheric parameters, including the abundance and stratigraphy of hydrogen in the surface, the presence of strong neutron absorbers such as Cl and Fe in the Martian rocks and soil, the presence of CO_2 ice on the surface, the column abundance of the atmosphere, and the enrichment and depletion of noncondensable gasses, N_2 and Ar, as CO_2 is cycled through the seasonal caps (Table 2). The effect of these parameters on the neutron counting rate can be explored using a simple physical model of the surface and atmosphere as described in Section 2.2 (Fig. 4a). Models of the counting rate are then used to develop algorithms to determine parameters from observations.

For example, the variation of thermal, epithermal, and fast neutron counting rates as a function of water abundance in a homogeneous surface is shown in Fig. 11a. Epithermal and fast neutrons are sensitive to hydrogen (as described in Section 2.2) and their counting rates decrease monotonically with water abundance. Both are insensitive to the abundance of elements in the surface other than hydrogen, as illustrated in Fig. 11a by changing the abundance of Cl, which is a strong thermal neutron absorber. In contrast, thermal neutrons are sensitive to variations in major-element composition and relatively insensitive to hydrogen when the abundance of WEH is less than about 10%. Epithermal neutrons are a good choice for determining the WEH abundance because of their high counting rate and relative insensitivity to other parameters. Measured

TABLE 2 **Sensitivity of neutron energy ranges to Mars surface and atmospheric parameters**

Type	Energy Range	Major interactions	CO_2-free surface parameters*	Atmospheric/seasonal parameters
Fast	>0.2 MeV	Inelastic scattering, elastic scattering	WEH abundance and stratigraphy, Average atomic mass	Atmospheric mass, CO_2 ice column abundance <100 g/cm^2
Epithermal	0.5 eV (Cd cutoff) to 0.2 MeV	Elastic scattering	WEH abundance and stratigraphy	Atmospheric mass, CO_2 ice column abundance up to about 150 g/cm^2
Thermal	<0.5 eV (Maxwellian energy distribution)	Elastic scattering, capture (absorption)	WEH abundance, Absorption by Fe, Cl, Ti. Stratigraphy of WEH and absorbers	CO_2 ice column abundance up to about 1000 g/cm^2, Absorption by N_2 and Ar

*The surface in the northern or southern hemisphere during summer following the recession of the seasonal cap.

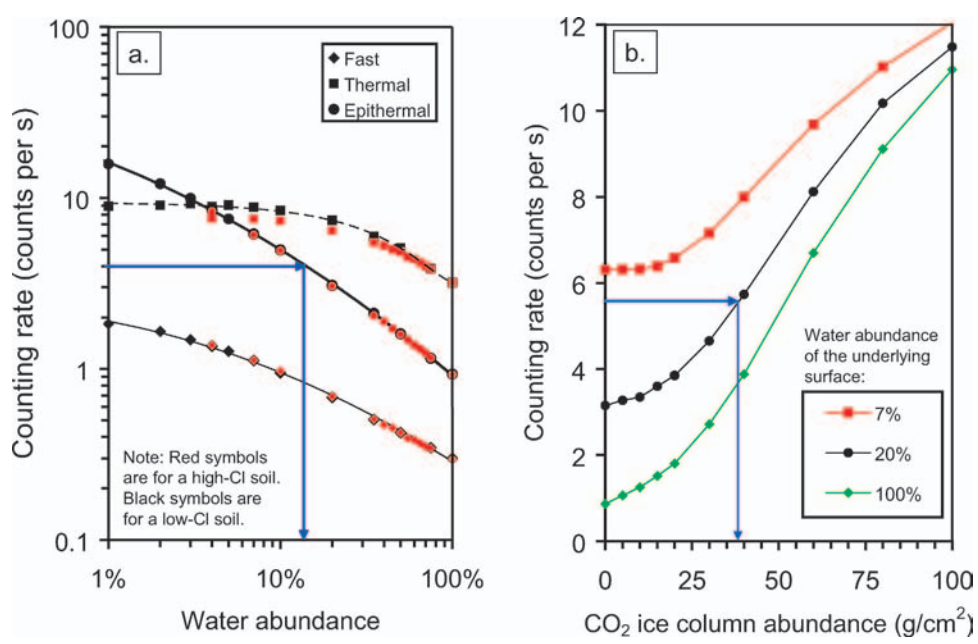

FIGURE 11 (a) Variation of thermal, epithermal, and fast neutron counting rates as a function of water abundance for a soil composition with low Cl abundance (black symbols). The red symbols correspond to a soil with higher Cl abundance, similar to the average composition of soils at the *Pathfinder* landing site. Note that the epithermal and fast neutron counting rates are unaffected by the change in Cl abundance. Because Cl is a strong absorber of thermal neutrons, the thermal neutron counting rate is sensitive to Cl abundance. (b) Variation of epithermal counting rate as a function of CO_2 ice column abundance covering homogeneous surfaces containing 7%, 20%, and 100% water ice (mixed with dry soil). Observed counting rates can be converted directly to water-equivalent hydrogen abundance or CO_2 ice column abundance using the model results in parts a and b as indicated by the arrows. The counting rate during the summer, which is a measure of the water abundance of the underlying surface, must be known in order to select the correct trend for CO_2 ice column abundance.

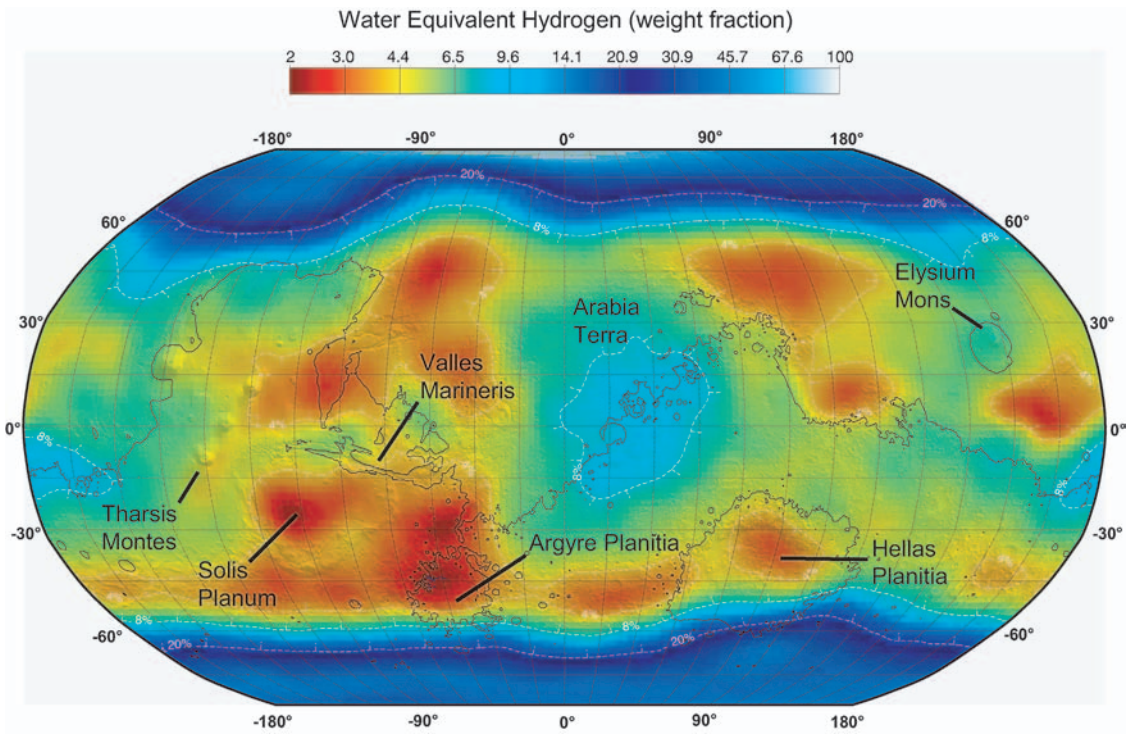

FIGURE 12 Global map of the abundance (weight fraction) of WEH. The map gives a lower bound on the abundance of WEH. Contours for 4%, 8%, and 20% WEH are shown as dashed white lines. The black contour line corresponds to 0 km elevation. The map data are superimposed on a shaded relief image. (Elevation data and shaded relief image courtesy of the NASA Mars Orbiter Laser Altimeter Science Team.)

epithermal counting rates can be converted directly to WEH as indicated by the arrows in Fig. 11a.

A map of WEH determined from measured epithermal counting rates is shown in Fig. 12. In order to avoid contributions from the seasonal CO_2 ice, the northern and southern high latitudes only included counting rates measured during their respective summers. The algorithm for determining WEH included corrections for minor variations in the counting rate due to changes in the atmospheric column abundance with topography. The map gives a lower bound on WEH. Higher WEH abundances could be present if the surface is stratified, for example, with a dry top layer covering a water-rich medium.

The minimum WEH abundance on Mars ranges from 2% in equatorial and midlatitude regions to nearly 100% for the north polar water-ice cap. Low abundances of WEH are found in regions such as northern Argyre Planitia, the midlatitude, southern highlands, Solis Planum, and the eastern flanks of the Tharsis Montes. Correlations between WEH and topography suggest that some aspects of the surface distribution of WEH can be explained by regional and global weather patterns. Moderate WEH abundances (8–10%) can be found in large equatorial regions, for example, in Arabia Terra. Ice stability models predict that water-ice is not stable at equatorial latitudes on Mars under present climate conditions. Consequently, the moderate abundances of WEH may be in the form of hydrated minerals, possibly as magnesium sulfate hydrate. High abundances of WEH are found at high northern and southern latitudes (poleward of 60°). A detailed analysis of neutron and gamma ray counting rates suggests that the high latitude surface outside of the residual caps consists of soil rich in water-ice covered by a thin layer of dessicated material (soil and rocks). This result is consistent with models that predict that water ice is stable at shallow depths at high latitudes. Similar terrestrial conditions are observed in the Dry Valleys of Antarctica, where ice is stable beneath a dry soil layer that provides thermal and diffusive isolation of the ice from the atmosphere.

Seasonal variations on Mars are driven by its obliquity relative to the orbital plane, which is similar to that of Earth. In the polar night in the northern and southern hemispheres, atmospheric CO_2 condenses to form ice on the surface. Approximately 25% of the martian atmosphere is cycled into and out of the northern and southern seasonal caps. Consequently, the seasonal caps play a major role in atmospheric circulation. The main questions about the seasonal caps that remain unanswered concern the local energy balance, polar atmospheric dynamics, and CO_2 condensation mechanisms. Seasonal parameters constrained by neutron spectroscopy include the column abundance of CO_2

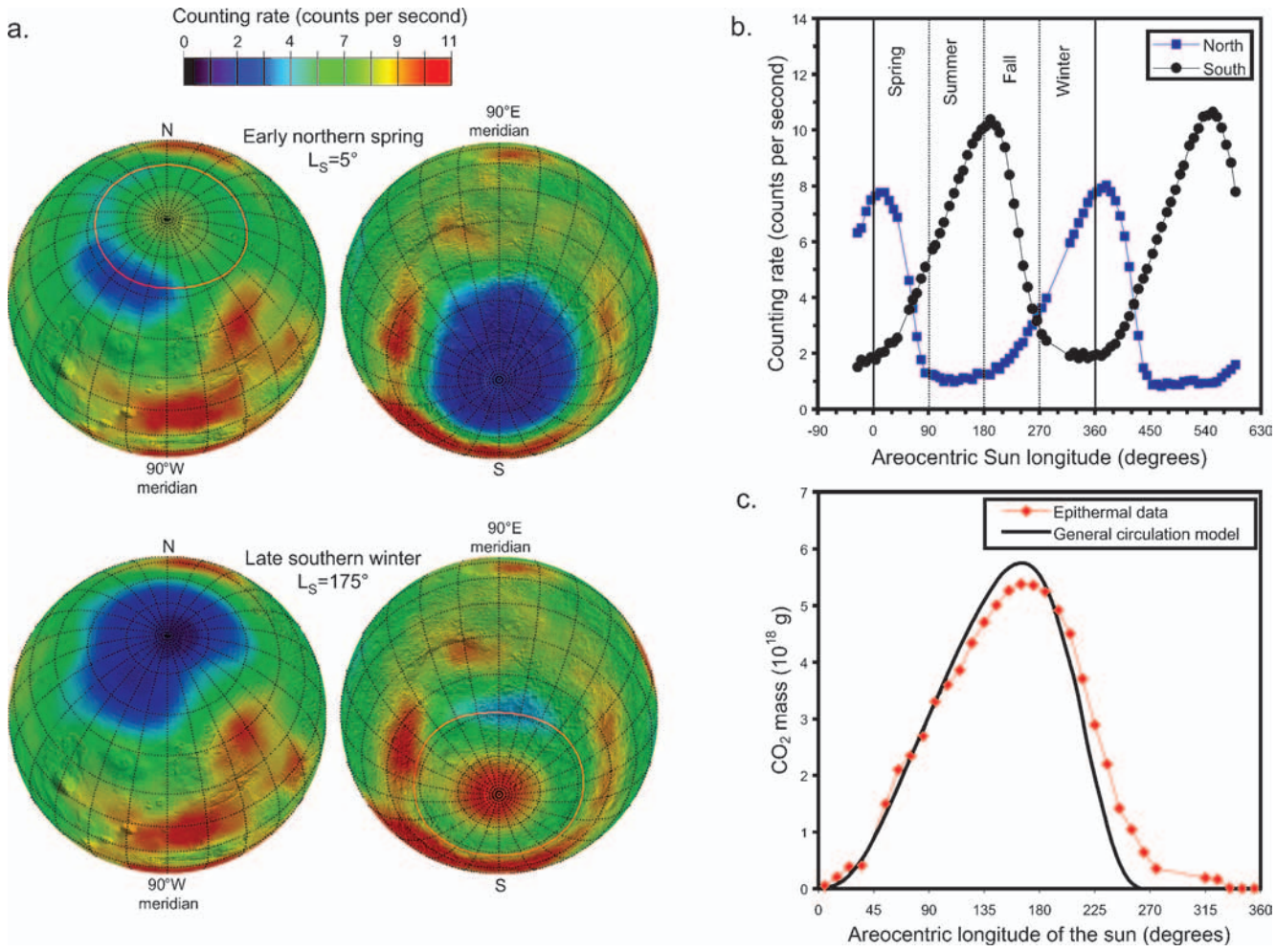

FIGURE 13 (a) Orthographic projections of epithermal counting rates in northern and southern hemispheres of Mars during early northern spring and late southern winter (red lines indicate the edge of the seasonal caps determined from data acquired from the MGS Thermal Emmission Spectrometer). Cap edge data provided by T. Titus of the USGS Astrogeology team. (b) Epithermal counting rate as a function of time at the north and south pole (poleward of 85°); (c) total mass of CO_2 in the southern seasonal cap poleward of 60°S from a general circulation model is compared to that determined from the epithermal counting data. (General circulation model results courtesy of NASA Ames Research Center and the New Mexico State University Department of Astronomy.)

ice on the surface and the column abundance of noncondensable gasses (N_2 and Ar) in the atmosphere. For example, analyses of gamma ray and neutron spectroscopy data reveal that the southern atmosphere is strongly enriched in N_2 and Ar during cap growth. The observed enrichment may be caused by the formation of a strong polar vortex accompanying the condensation flow, which inhibits **meridional mixing** of the polar atmosphere with lower latitudes.

Based on simulations, the epithermal neutron counting rate generally increases with the column abundance of CO_2 ice on the surface; however, the trend depends on the abundance of water ice in the underlying surface as is shown in Fig. 11b. The sensitivity of epithermal neutrons to CO_2 ice is higher for surfaces that contain more water ice. At high latitudes, the column abundance of CO_2 can be determined from seasonal epithermal counting rates, given the counting rate during summer, when no CO_2-ice is present.

Maps of epithermal counting rates are shown in Fig. 13a. The extent of the seasonal caps can be seen by comparing maps of the northern and southern hemispheres during the two time periods shown in Fig. 13a. For example, during late southern winter, low counting rates are observed in the northern high latitudes, corresponding to the summertime CO_2 frost-free surface, which contains abundant water ice. In early northern spring, elevated epithermal counting rates are observed in the northern hemisphere, corresponding to CO_2 ice on the surface.

During their respective winters, the counting rate at high latitudes increases towards the poles, which indicates that the CO_2 ice column abundance increases with latitude. The observed spatial variation is expected since the polar night lasts longer at higher latitudes and frost has more time to accumulate. The time variation in epithermal counting rates for the north and south poles (poleward of 85°), shown in Fig. 13b, reveals the cyclic behavior of the seasonal caps during two Mars years. The total inventory of CO_2 in the seasonal caps determined from epithermal counting data is similar to that predicted by general circulation models (GCMs) (for example, see Fig. 13c). The ability to measure the thickness of the CO_2 caps in the polar night is unique to gamma ray and neutron spectroscopy. Local ice column abundances determined by nuclear spectroscopy can be compared to GCM predictions, providing information needed to improve physical models of the seasonal caps and the polar energy balance.

6. Future Prospects

Given the number of orbiters, landers, and rovers targeting Mars and the renewed emphasis on lunar exploration, the Moon and Mars will be the focus of planetary science for years to come. On the Moon, neutron spectrometers may be used on rovers or incorporated into borehole logging tools to search for and characterize water-ice deposits in polar craters. On Mars, gamma ray and neutron spectrometers may be included on rovers, landers, weather stations, and drilling systems for *in situ* determination of composition, for example, to investigate small spatial scale variations in composition and to look for water deep within the Martian surface. In addition, there may be opportunities for low-altitude, high-spatial resolution measurements of selected regions from an airplane or balloon platform. Continued effort is needed to analyze and interpret data already acquired by *Lunar Prospector* and *Mars Odyssey* and to synthesize the information with other data sets to develop a coherent picture of the Moon and Mars. Orbital nuclear spectroscopy will also play an important role on future solar system exploration missions. For example, the *MESSENGER* mission to Mercury and the *Dawn* mission to the main asteroid belt include gamma ray and neutron spectrometers on their payloads.

Bibliography

Boynton, W. V., et al. (2004). The Mars Odyssey gamma-ray spectrometer instrument suite. *Space Science Rev.* **110**, 1–2, 37–83.

Duderstadt, J. J., and L. J. Hamilton (1967). "Nuclear Reactor Analysis" John Wiley & Sons.

Elphic, R. C., et al. (2002). Lunar Prospector neutron spectrometer constraints on TiO2. *J. Geophys. Res.* **107**, E4, 5024, 10.1029/2000JE001460.

Feldman, W. C., et al. (2001). Evidence for water ice near the lunar poles. *J. Geophys. Res.* **106**, 23, 231–23, 251.

Feldman, W. C., et al. (2004). Gamma-ray, neutron, and alpha-particle spectrometers for the Lunar Prospector mission. *J. Geophys. Res. Planets*. **109**, E7, p. E07S06.

Feldman, W. C., et al. (2004). Global distribution of near-surface hydrogen on Mars. *J. Geophys. Res. Planets*. **109**, E9, p E09006.

Knoll, G. F. (1989). "Radiation detection and measurement" 2nd edition, John Wiley & Sons.

Lawrence, D. J., et al. (2000). Thorium abundances on the lunar surface. *J. Geophys. Res.* **105**(E8), 20, 307–20, 331.

Lawrence, D. J., et al. (2002). Iron abundances on the lunar surface as measured by the Lunar Prospector gamma-ray and neutron spectrometers. *J. Geophys. Res*. **107**(E12), 5130, doi:10.1029/2001JE001530.

Pieters, C. M., and P. A. J. Englert, Eds. (1993). "Remote Geochemical Analysis: Elemental and Mineralogical Composition" Cambridge University Press.

Prettyman, T. H., et al. (2004). Composition and structure of the Martian surface at high southern latitudes from neutron spectroscopy. *J. Geophys. Res*. **109**, p. E05001, doi:10.1029/2003JE002139.

Prettyman, T. H., et al. (2006). Elemental composition of the lunar surface: Analysis of gamma ray spectroscopy data from Lunar Prospector. *J. Geophys. Res.* **111**, doi:10.1029/2005JE002656, in press.

Reedy, R. C. (1978). Planetary gamma-ray spectroscopy. Proceedings of the 9th Lunar and Planetary Science Conference, pp. 2961–2984.